Continental Shelf Research 193 (2020) 104035

Contents lists available at ScienceDirect

Continental Shelf Research

journal homepage: http://www.elsevier.com/locate/csr

Research papers

Observational study of tidal mixing asymmetry and eddy viscosity-shear covariance - induced residual flow in the Jiulong River estuary

Peng Cheng [a,*], Fengling Yu [a], Nengwang Chen [b], Aijun Wang [c]

[a] State Key Laboratory of Marine Environment Science, College of Ocean and Earth Sciences, Xiamen University, Xiamen, Fujian Province, 361102, China
[b] Fujian Provincial Key Laboratory for Coastal Ecology and Environmental Studies, College of the Environment and Ecology, Xiamen University, Xiamen, Fujian Province, 361102, China
[c] Third Institute of Oceanography, Ministry of Natural Resources, Xiamen, Fujian Province, 361005, China

ARTICLE INFO

Keywords:
Estuarine circulation
Tidal mixing asymmetry
ESCO flow
ADCP variance method
Lateral circulation
Jiulong river estuary

ABSTRACT

An observation study was conducted at three stations in the inner regime of the Jiulong River estuary to examine the tidal mixing asymmetry and its associated residual flow induced by eddy viscosity-shear covariance (ESCO). The water columns at the observation stations were approximately well-mixed during the later flood and were stratified during the early ebb, a typical tidal mixing asymmetry. Corresponding to the tidal variation of stratification, the Reynolds stress and vertical eddy viscosity, which were obtained using the ADCP variance method, exhibited distinct differences in the magnitude and vertical structure between flood and ebb tides. The ESCO flow was calculated using the decomposition method for estuarine circulation, revealing a two-layer vertical structure similar to density-driven flow but with a much greater magnitude, confirming the findings of previous generic model studies that the ESCO flow dominates the density-driven flow in periodically stratified estuaries. The drivers of tidal mixing asymmetry were explored using the potential energy anomaly method. Longitudinal straining reduced stratification during flood tides and reinforced stratification during ebb tides, whereas longitudinal advection acted in the opposite manner. Although the contribution of lateral circulation to stratification was neglected due to the lack of lateral observation data, scaling analysis revealed that lateral advection was important in the longitudinal dynamics and tidal evolution of stratification and warrants further study.

1. Introduction

Estuarine circulation is one of the most studied topics in estuarine physics. According to traditional theory, the residual circulation is the sum of the runoff and the flow driven by the longitudinal density gradient (i.e., the density-driven flow), and is also known as gravitational circulation (Pritchard, 1956; Hansen and Rattray, 1965). The longitudinal momentum balance that determines the gravitational circulation is between the baroclinic pressure and residual water level gradients and the vertical divergence of shear stress:

$$0 = -g\frac{\partial\langle\eta\rangle}{\partial x} + \frac{g}{\rho_0}\frac{\partial\langle\rho\rangle}{\partial x} + \frac{\partial}{\partial z}\left(K_m\frac{\partial\langle u\rangle}{\partial z}\right), \quad (1)$$

where g is gravitational acceleration, the angle brackets indicate the tidal average, η is the water surface elevation, ρ is the water density, ρ_0 is a reference water density, u is the longitudinal (or along-estuary) velocity (x direction), z represents the vertical direction, and K_m is the vertical eddy viscosity, which is parameterized with a constant effective vertical eddy viscosity. Jay and Muziak (1994) found that the vertical mixing undergoes remarkable tidal fluctuations, which are typically larger during flood than during ebb (this is also referred to as tidal mixing asymmetry), and proposed that the temporal covariance between the fluctuations in K_m and the velocity shear, i.e., $\widetilde{K_m}\frac{\partial\tilde{u}}{\partial z}$, where $u = \langle u\rangle + \tilde{u}$ and $K_m = \langle K_m\rangle + \tilde{K_m}$), can generate a residual flow that constitutes a main component of the estuarine circulation.

To examine the conceptual model of the residual flow driven by tidal mixing asymmetry, a series of generic modeling studies have been conducted. Burchard and Hetland (2010) showed that the residual flow is twice the magnitude of the density-driven flow in periodically stratified estuaries using idealized numerical experiments. Cheng et al. (2010) provided a two-dimensional analytical solution for the residual flow, which showed that substantial asymmetric mixing between flood and ebb tides leads to stronger residual flow and reversed tidal mixing asymmetry generates a residual flow with an opposite vertical structure

* Corresponding author.
E-mail address: pcheng@xmu.edu.cn (P. Cheng).

https://doi.org/10.1016/j.csr.2019.104035
Received 24 April 2019; Received in revised form 3 December 2019; Accepted 5 December 2019
Available online 7 December 2019

to that driven by typical tidal mixing asymmetry. These generic studies also indicated that the strength of flow induced by tidal mixing asymmetry depends on the Simpson number, confirming that strain-induced periodic stratification (Simpson et al., 1990) is an important physical mechanism in creating the tidal variation of vertical mixing. Therefore, the residual flow has been referred to as tidal straining-induced flow (Burchard and Hetland, 2010) or asymmetric tidal mixing induced flow (Cheng et al., 2010). Subsequent studies further revealed that various processes can generate the variations in tidal mixing. Burchard and Schuttelaars (2012) found that lateral advection plays a key role in creating the asymmetry of current velocity shear between flood and ebb tides. To generalize the processes that generate the eddy viscosity-shear covariance (ESCO) term, Dijkstra et al. (2017) referred to the residual flow as ESCO flow and further decomposed the ESCO term and identified four mechanisms involving direct and indirect interactions of the time-varying eddy viscosity with the tidal current and gravitational residual current. Chen and de Swart (2018) analyzed the influences of along-estuary bottom slope and tidal constituents on ESCO flow and showed that the magnitude and vertical structure of ESCO flow are dependent on the mixture of diurnal, semi-diurnal and quarter-diurnal tides.

In situ observations of tidal mixing asymmetry have been conducted in estuaries and on shelves. Using the acoustic Doppler current profiler (ADCP) variance method, Simpson et al. (2005) obtained shear stress and vertical eddy viscosity profiles for the York River estuary. The results clearly demonstrated higher eddy viscosities during flood tides than ebb tides and revealed the major role of tidal straining in controlling the structure and intensity of turbulent stresses and turbulence kinetic energy production during both the ebb and flood phases of the tide. Becherer et al. (2011) performed a micro-structure profiler observation in the Wadden Sea and obtained evidence of the effects of tidal straining on tidal mixing asymmetry, i.e., high values of viscous dissipation observed during the flood tide and lower values observed during the ebb tide. Although tidal mixing asymmetry was evident in these observations, the associated residual flow (i.e., the ESCO flow) has not been directly investigated. The main objectives of this study were to explore the ESCO flow using observed data from a tidally energetic estuary and examine the findings drawn from previous generic models of ESCO flow.

The remainder of this paper is structured as follows. In section 2, the study site, observed data, and ADCP variance method are described. In section 3, the observed data are used to (1) present the characteristics of tidal current velocity and stratification, (2) estimate the vertical eddy viscosity, and (3) calculate the ESCO flow. In section 4, the discussion focuses on (1) the limitations of the ADCP variance method, (2) drivers of tidal mixing asymmetry, and (3) the role of lateral circulation in estuarine dynamics. Section 5 summarizes the main findings of this study.

2. Data and methods

2.1. Study site and observation campaign

The study site was the Jiulong River estuary, which is located on the western side of the Taiwan Strait along the southeast coast of China (Fig. 1a). The bathymetry of the estuary is complex, with extensive islands and intertidal mudflats in the middle of the estuary (see the regions above the 0 m isobars in Fig. 1), which shelter the estuary from wave activities propagating from the ocean. The water depth is generally less than 15 m. The major tidal constituent is M_2. The mean tidal range is 3.9 m and the maximum range was reported to be 6.4 m (Jiang and Wai, 2005; Wang et al., 2013). The estuary has two large tributaries, namely, the North Stream and West Stream. The mean annual water discharge is 1.24×10^{10} m^3, with approximately 70% of the total discharge occurring between April and September (the wet season), when typhoons frequently occur. During the dry season (November to February of the next year), the discharge is approximately 15–20% less than the annual mean (Liu et al., 1994).

The observations were performed during 6–8, May 2015 at three stations along the south coast, which is the main navigation channel of the estuary (Fig. 1b). At each station, a bottom-mounted ADCP was deployed and a boat was anchored nearby. For the turbulence measurements, the Workhorse instrument (1200 kHz) was used with sampling at a ping rate of 0.5 Hz and a vertical bin size of 0.25 m. For the temperature and salinity measurements, the Sea & Sun Technology CTD 48M probe was used and 40 CTD profiles were obtained hourly from the anchored boat. The width of the south channel where the observations were undertaken is approximately 300 m. During the observation period, the river discharge into the south channel was approximately 300 m^3/s and the tidal range was about 5 m, a typical tide for the estuary.

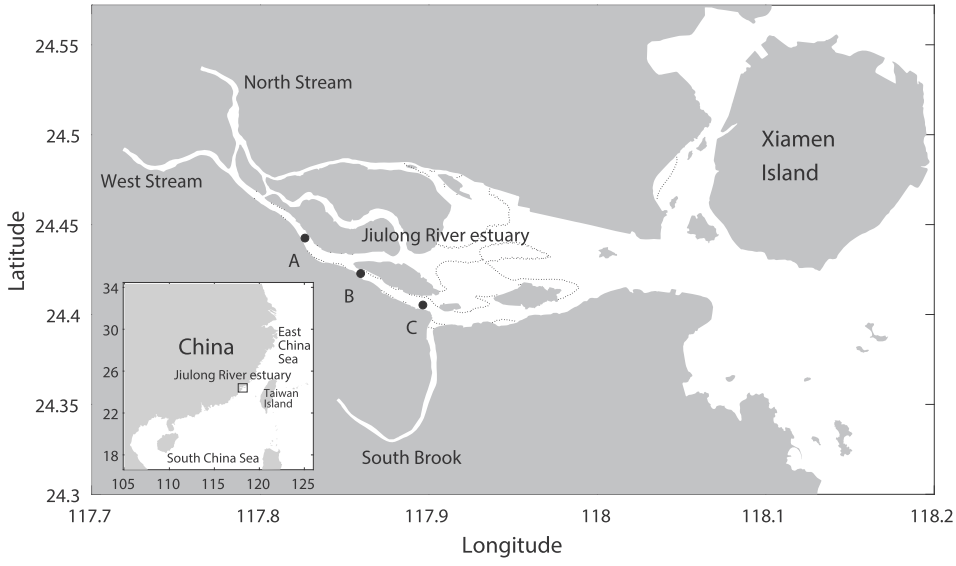

Fig. 1. Main body and location (the box in the inset) of the Jiulong River estuary. The solid dots indicate the observation stations and the contours represent 0 m isobars.

2.2. Methods

2.2.1. Preprocessing of the ADCP data

Due to malfunction of the ADCP at station A, velocity data were only obtained at stations B and C and were rotated in the along- (x) and cross-estuary (y) directions using the principal component analysis method. In the rotated coordinates, the x extends toward the sea and the y coordinate is to the left of x (i.e., it directs toward the right bank, facing upstream of the estuary). The data with "Percent Good" smaller than 80 or autocorrelation less than 110 dB were removed and replaced using spline interpolation. The top blank layer of the velocity measurements was discarded and the bottom 1.3 m blank layer was filled by extrapolation with the logarithmic velocity profile. The extrapolation of the Reynolds stress in the bottom blank layer was performed as described by Stacey and Ralston (2005) by assuming a linear distribution of the Reynolds stress profile in the bottom boundary layer (BBL):

$$-\overline{u'w'}(z) = u_*^2\left(1-\frac{z}{h_{BBL}}\right), \tag{2}$$

where the overbar indicates the average over a time interval (10 min), the prime symbol denotes the departure from the time mean, $-\overline{u'w'}(z)$ is the Reynolds stress profile obtained using the ADCP variance method (for the details, see the following section), z is the height above the bed, u_* is the bottom friction velocity, and h_{BBL} is the height of the BBL. Fitting Eq. (2) to each profile of the Reynolds stresses (using the profile data for the lower half) results in the two boundary-layer parameters, u_* and h_{BBL}. Only the fittings with correlation coefficients (R^2) greater than 0.5 within the BBL were used to estimate u_*^2. Approximately 70% of the profiles at station B and 35% of the profiles at station C (where stronger stratification reduces the applicability of Eq. (2)) were valid. For the invalid profiles, u_*^2 was linearly interpolated from estimates of the adjacent time steps.

2.2.2. Reynolds stress and vertical eddy viscosity

Estimates of the components of Reynolds stress $-\overline{u'w'}$ and $-\overline{v'w'}$ were made on the basis of the variance method (Stacey et al., 1999a; Lu and Lueck, 1999b):

$$\frac{-\overline{u'w'} = \overline{b_2'^2} - \overline{b_1'^2}}{4sin\theta cos\theta}, \tag{3a}$$

$$\frac{-\overline{v'w'} = \overline{b_4'^2} - \overline{b_3'^2}}{4sin\theta cos\theta}, \tag{3b}$$

where b_i denotes the velocity along the ith ($i = 1,\cdots,4$) beam and θ is the angle each beam of the ADCP makes with the vertical direction ($\theta = 20^\circ$ for the RDI Workhorse used here).

The rate of shear production was obtained from the product of stress and shear as

$$P = -\overline{u'w'}\frac{\partial u}{\partial z} - \overline{v'w'}\frac{\partial v}{\partial z}, \tag{4}$$

where u and v are the average velocities over 10 min. The vertical eddy viscosity (K_m) was calculated from the shear production rate and the magnitude of shear (S),

$$K_m = \frac{P}{S^2} \tag{5a}$$

$$S^2 = \left(\frac{\partial u}{\partial z}\right)^2 + \left(\frac{\partial v}{\partial z}\right)^2 \tag{5b}$$

The estimates of K_m are subject to large uncertainties, particularly for small magnitudes of shear. Negative shear production rates (hence negative eddy viscosities) were observed near the surface, especially during slack water periods, resulting from measurement errors or possible counter-gradient momentum fluxes. These negative eddy viscosities were removed and filled by vertical interpolation using spline method. Because the mixing was weak during the slack water periods, the interpolation of negative eddy viscosities did not distort the tidal variation of eddy viscosity.

2.2.3. Decomposition of estuarine circulation

Estuarine circulation includes multiple components and can be decomposed corresponding to different driving mechanisms. Because the south channel of the Jiulong River estuary is very narrow, the cross-estuary momentum equation can be decoupled from the along-estuary momentum equation and, therefore, the method of Cheng et al. (2013) was applied. The ESCO ($\langle u\rangle_{ESCO}$), density-driven ($\langle u\rangle_D$), River discharge-induced ($\langle u\rangle_R$), and Stokes return flows ($\langle u\rangle_S$) were computed. Here, only the solution for the ESCO flow is presented and the methods and results that describe the other flow terms can be found in Cheng et al. (2013):

$$\langle u\rangle_{ESCO} = \frac{g}{\langle Z\rangle}\frac{\partial\langle\eta\rangle_{ESCO}}{\partial x}\int_{\sigma}^{0}\frac{\sigma'}{\langle K_m\rangle}d\sigma' - \frac{1}{\langle Z\rangle}\int_{-1}^{\sigma}\frac{1}{\langle K_m\rangle}\left(ESCO - \int_{\sigma'}^{0} ESCO_\sigma d\sigma''\right)d\sigma', \tag{6a}$$

$$ESCO = \langle Z\rangle\left\langle \tilde{K}_m\partial\frac{\tilde{u}}{\partial\sigma'}\right\rangle, \tag{6b}$$

$$ESCO_\sigma = \frac{1}{\langle Z\rangle}\int_{\sigma'}^{0}\left[\left\langle \tilde{Z}\frac{\partial}{\partial\sigma''}\left(K_m\partial\frac{\tilde{u}}{\partial\sigma''}\right)\right\rangle + \left\langle \tilde{Z}\frac{\partial}{\partial\sigma''}\left(\tilde{K}_m\frac{\partial u}{\partial\sigma''}\right)\right\rangle + \left\langle \tilde{Z}\frac{\partial}{\partial\sigma''}\left(\tilde{K}_m\partial\frac{\tilde{u}}{\partial\sigma''}\right)\right\rangle\right]d\sigma'', \tag{6c}$$

$$\frac{\partial\langle\eta\rangle_{ESCO}}{\partial x} = \frac{\int_{-1}^{0}\int_{-1}^{\sigma}\frac{1}{\langle K_m\rangle}\left(ESCO - \int_{\sigma'}^{0} ESCO_\sigma d\sigma''\right)d\sigma' d\sigma}{g\int_{-1}^{0}\int_{\sigma}^{0}\frac{\sigma'}{\langle K_m\rangle}d\sigma' d\sigma}, \tag{6d}$$

where $\sigma = (z-\eta)/D$ is the non-dimensional vertical direction, $D = \eta + H$, H is the undisturbed water depth, and $1/D^2 = \langle Z\rangle + \tilde{Z}$. The sigma coordinates were used to overcome the difficulty of calculating tidally averaged quantities in a surface layer influenced by tidal fluctuations of water level. Eq. (6c) arises from the sigma coordinate transformation and is part of the ESCO.

To calculate the tidal mean and fluctuation of velocity and eddy viscosity, the first two tidal cycles (6 May 2015 22:00 to 7 May 2015 23:00) identified from the depth mean velocity were selected. The longitudinal density gradients at stations B and C were computed based on the CTD data at the three stations. It was noted that the maximum bottom salinity coincided with the high water elevation at stations A and C but was delayed by 1 h at station B (Fig. 2c and d). To take into account

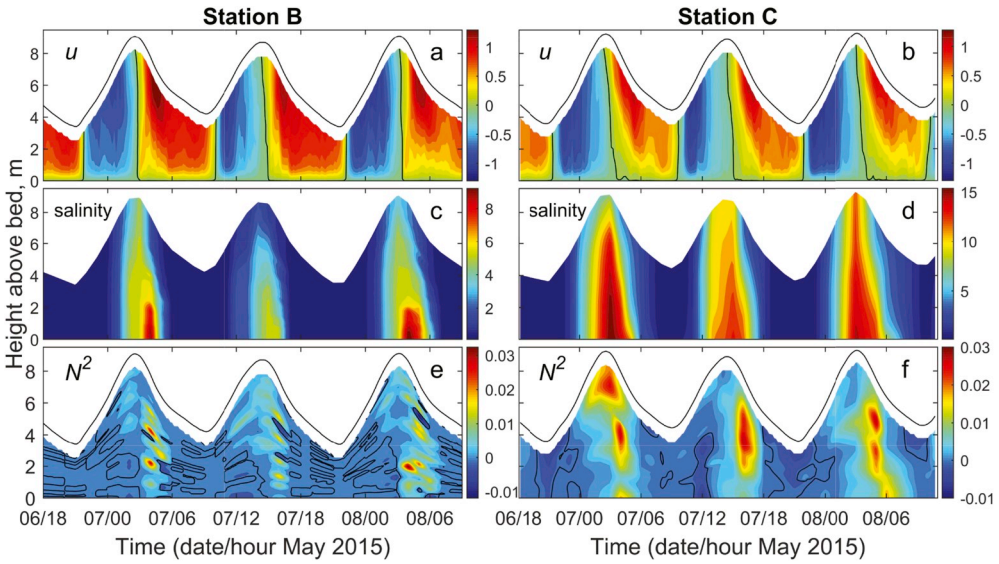

Fig. 2. Temporal variations in profiles of longitudinal velocity in units of m/s (u, upper panel), salinity in units of PSU (middle panel), and buoyancy frequency in units of 1/s (N^2, bottom panel) at stations B (left column) and C (right column). Positive values of velocity represent seaward currents. The black contours in a, b, e, and f indicate a value of 0. The negative values of N^2 result from brief temperature inversion.

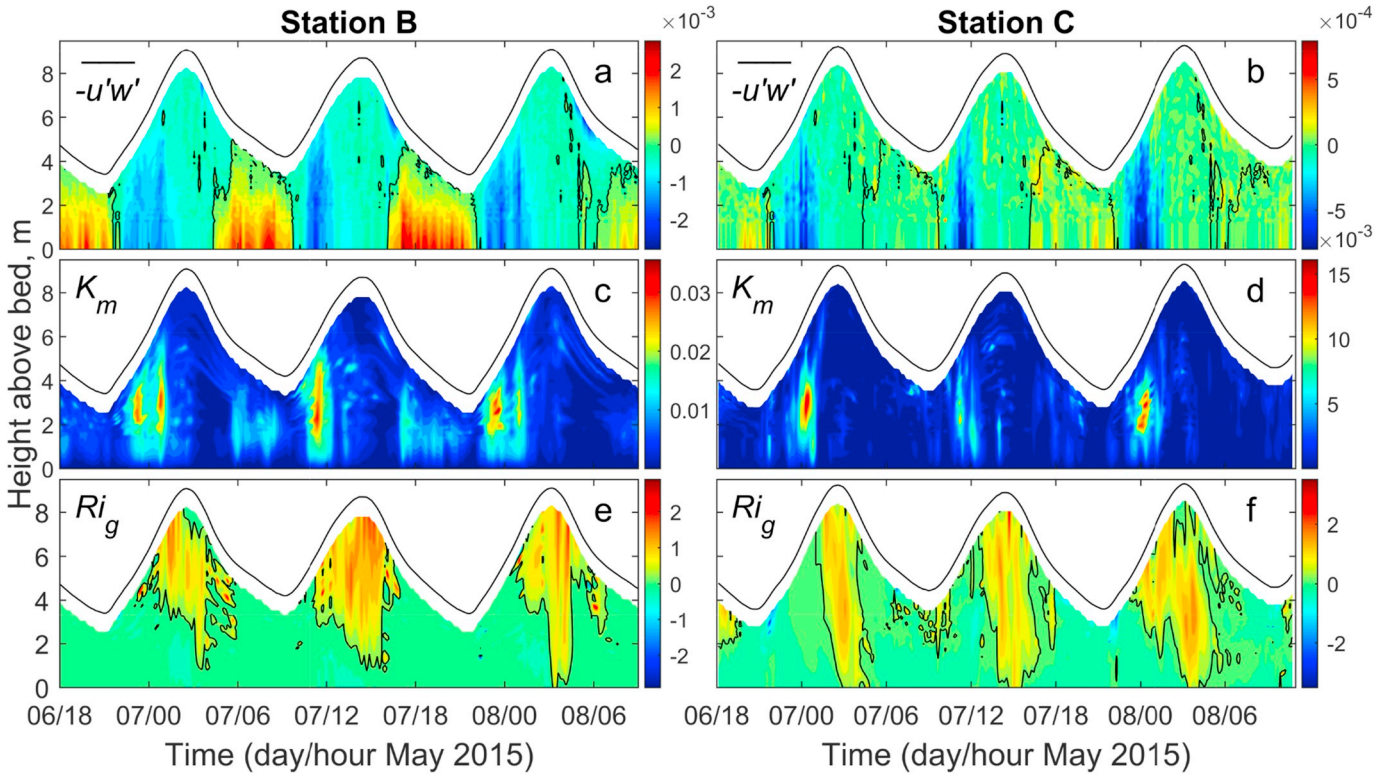

Fig. 3. Temporal variations in profiles of longitudinal Reynolds stress in units of N/m^2 (upper panel), vertical eddy viscosity in units of m^2/s (middle panel), and gradient Richardson number at stations B (left column) and C (right column). Positive values of the Reynolds stresses represent seaward stresses. The black contours in a and b indicate a value of 0, and in e and f indicate a value of 0.25.

this different salinity evolution, a forward difference scheme was used to calculate the density gradients; for station B, $\frac{\partial \rho}{\partial x} = \frac{\rho_C - \rho_A}{\Delta x_{AC}}$, and for station C, $\frac{\partial \rho}{\partial x} = \frac{\rho_C - \rho_B}{\Delta x_{BC}}$. Here, Δx is the longitudinal distance between two stations.

3. Results

3.1. Tidal currents and stratification

The tidal waves in the estuary are approximately standing waves with the maximum flood and ebb tides occurring around the mean water

level (Fig. 2a and b). The magnitude and duration were longer during ebb than during flood tides, indicating an ebb-dominant tide. At station B, the mean current velocity was 0.59 m/s during the flood and 0.70 m/s during the ebb. At station C, the tidal asymmetries in current velocity and duration were relatively less pronounced. The generation of the ebb-dominant tide is attributable to two main processes: (1) the extensive intertidal flats store water during flood tides and release water to the channel during ebb tides, producing a longer ebb in the channel, as described by Friedrichs and Aubrey (1988); (2) the river discharge produces a non-negligible barotropic flow that reinforces ebb tides. The vertical profile of the tidal current velocity was also asymmetric, with weaker shear during flood and stronger shear during ebb tides, reflecting the influence of stratification on the tidal current velocity profile (Jay, 1991).

Because the two stations are located in the inner regime of the estuary, saltwater appeared only during the high-water period and freshwater dominated the low-water period, resulting from the migration of the seawater/freshwater interface (or front). The stratification was relatively weak during the later flood and stronger during the early ebb, showing typical tidal mixing asymmetry during the high-water period. The pattern of buoyancy frequency ($N^2 = -\frac{g}{\rho_0}\frac{\partial \rho}{\partial z}$) was consistent with the tidal variation of stratification and further indicated that elevated stratification occurred in the middle water column during the early ebb. Station C exhibited higher salinity and stronger stratification than station B due to its proximity to the mouth of the estuary. Several cases of overturning, indicated by negative values of N^2, were also observed during the low water period (Fig. 2f).

3.2. Reynolds stress and vertical eddy viscosity

The Reynolds stress was large near the bottom during both the flood and ebb phases of the tidal flow (Fig. 3a and b). During the high-water period, the Reynolds stress was low resulting from the combined effects of slack water and stratification. The magnitude of the Reynolds stress was lager during ebb than during flood tides at station B, whereas the opposite trend was observed at station C. In general, the strength of the Reynolds stress at station B was one order of magnitude greater than that at station C. The Reynolds stress profiles revealed distinct differences in magnitude and structure between floods and ebbs (Fig. 4). At station B, during flood tides, the profiles were almost linear throughout the entire water column, whereas during ebb tides, the Reynolds stress was weak in the upper 4 m and thereafter linearly increased toward the bottom. These Reynolds stress profiles during ebb tides indicated nearly inviscid condition in the upper water column and suggested that the boundary-generated stress did not reach the surface during this phase of the tide. The tidal variation of Reynolds stress is similar to those found in the Hudson River estuary (Geyer et al., 2000) and the York River estuary (Simpson et al., 2005), showing that stratification reduces the Reynolds stress near the surface. At station C, the Reynolds stress profiles were generally linear distribution during flood tides but showed a less clear structure during ebb tides, possibly because the measurements of Reynolds stress and eddy viscosity were less reliable. The relatively strong stratification at station C might be responsible for these low-quality results, and a detailed discussion of the limitations of the ADCP variance method is provided in section 4.1. Hereinafter, the analysis of the tidal mixing asymmetry and ESCO flow focuses on station B, and the results for station C are given as a reference.

The vertical eddy viscosities at the two stations showed a quarter-diurnal pattern apparent with high values during the flood tide reaching peak values in the middle of the water column and low values during the ebb tide (Fig. 3c and d). The temporal variation of the eddy viscosity indicated the occurrence of typical tidal mixing asymmetry. The eddy viscosity was low during the high-water period due to the weak flow and stratification. The highest eddy viscosity appeared at the maximum flood tide that was associated with a moderately well-mixed water column, whereas stratification reduced the mixing at the maximum ebb tide even though the tidal currents were strong. The observation in the York River estuary showed a similar tidal asymmetry of eddy viscosity with larger eddy viscosities appeared during flood than ebb tides, and also showed that the relatively strong stratification during the neap tide suppressed the vertical mixing leading to small eddy viscosities (Simpson et al., 2005). The vertical profiles of the eddy viscosity showed an asymmetric parabolic distribution with the maximum value close to the bottom (Fig. 5). The deviation from a parabolic profile (i.e., a neutral viscosity profile of open-channel flow) was likely attributable to the influence of stratification, which led to apparent attenuation near the surface. This result is consistent to the eddy viscosity profiles found in the Hudson River estuary (Geyer et al., 2000). At the maximum ebb tide, the eddy viscosity tended toward zero in the upper 4 m at station B, in accordance with the low shear stress, and was small and had an unclear

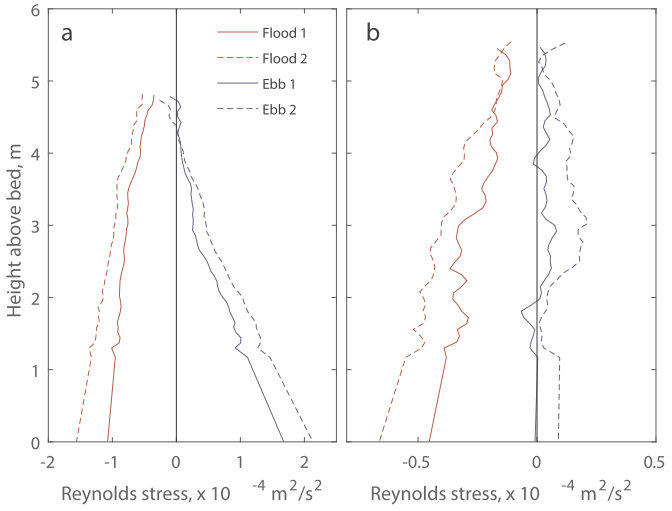

Fig. 4. Vertical profiles of Reynolds stress averaged over 30 min for the maximum flood and ebb tides at stations B (a) and C (b). At station B, flood 1 is chosen at 6 May 23:30, flood 2 is chosen at 7 May 11:30, ebb 1 is chosen at 7 May 6:00, and ebb 2 is chosen at 7 May 17:30. At station C, flood 1 is chosen at 6 May 23:00, flood 2 is chosen at 7 May 11:00, ebb 1 is chosen at 7 May 5:30, and ebb 2 is chosen at 7 May 17:00.

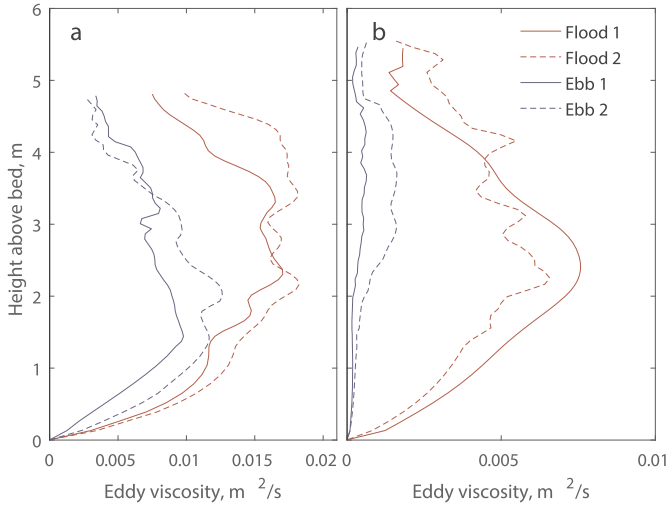

Fig. 5. Vertical profiles of vertical eddy viscosity for the maximum flood and ebb tides at stations B (a) and C (b). At station B, flood 1 is chosen at 6 May 23:30, flood 2 is chosen at 7 May 11:30, ebb 1 is chosen at 7 May 6:00, and ebb 2 is chosen at 7 May 17:30. At station C, flood 1 is chosen at 6 May 23:00, flood 2 is chosen at 7 May 11:00, ebb 1 is chosen at 7 May 5:30, and ebb 2 is chosen at 7 May 17:00.

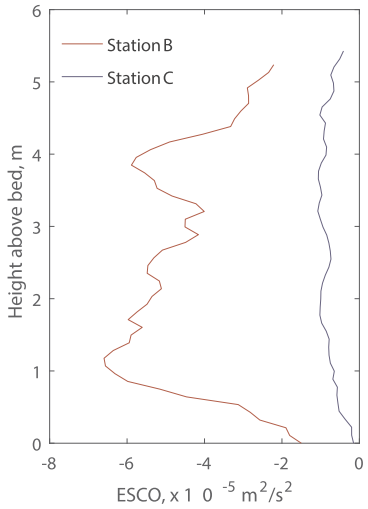

Fig. 6. Vertical profiles of ESCO term at stations B and C over the period from 6 May 22:00 to 7 May 23:00.

structure at station C.

The gradient Richardson number ($Ri_g = N^2/S^2$) distribution showed high Richardson numbers in the surface layer mostly during the high-water period (Fig. 3e and f), indicating stable conditions in the upper water column ($Ri_g > 0.25$). Low Richardson numbers occurred during the low-water periods, which is consistent with the greater values of eddy viscosity during those times. At station C, high Richardson numbers were observed for the upper water column under most tidal conditions, indicating relatively strong stratification at this station.

3.3. Residual flow

The ESCO represents the driving force of ESCO flow. According to Eq. (6a), the sign of the ESCO term (i.e., $ESCO - \int_\sigma^0 ESCO_\sigma d\sigma$' because of the sigma coordinate transformation) determines the direction of ESCO flow. Note the negative sign before the second term on the right-hand side of Eq. (6a). Negative values of the ESCO term drive seaward flow, acting in the opposite way to the longitudinal density gradient. The ESCO term at the two stations has negative values (Fig. 6), which is consistent with the findings from idealized numerical experiments (Cheng et al., 2013). The magnitude of the ESCO term was larger at station B than at station C, although the ESCO flow was stronger at station C (Fig. 7) because the flow strength is inversely related to the tidal mean eddy viscosity (Eq. (6a)), which was very low at station C.

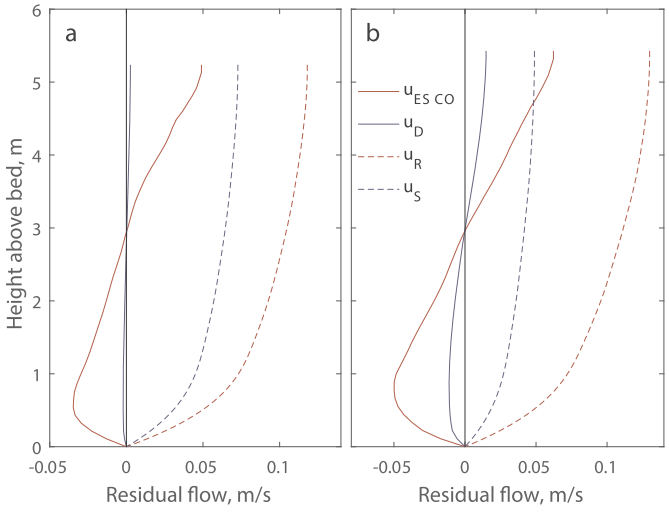

Fig. 7. Vertical profiles of ESCO flow (u_{ESCO}), density-driven flow (u_D), river-induced flow (u_R) and Stokes return flow (u_S) at stations B (a) and C (b).

Being balanced by the corresponding barotropic force, the ESCO flow exhibited a two-layer structure with seaward flow near the surface and landward flow near the bottom (Fig. 7). This flow pattern was similar to that of the density-driven flow, indicating that the ESCO flow reinforced the two-layer estuarine circulation. Because of the weak longitudinal density gradient in the inner regime of the estuary, the density-driven flow was weaker than the ESCO flow, which is consistent with the results of the generic studies of periodically stratified estuaries (e.g., Burchard and Hetland, 2010; Cheng et al., 2010, 2013). The magnitudes of the ESCO flow were similar at the two stations. The depth-averaged absolute values of the flow were 2.2 and 3.1 cm/s for stations B and C, respectively. The density-driven flow, however, was much stronger at station C than B, as a result of the lower eddy viscosity and greater along-estuary density gradient.

The decomposition method also provided the solutions of the Stokes return and river-induced flows (Fig. 7). The two flows were unidirectional with similar vertical profiles. The river-induced flow was the dominant component of those flows, and the Stokes return flow was comparable to the ESCO flow. Although the advection-induced flow was not available, the total residual flow at the two stations was likely seaward. Therefore, the residual dynamics in the inner regime of an estuary are quite distinct from the well-examined central regime: tidal rectification rather than the longitudinal density gradient is the main driving force of estuarine circulation.

4. Discussion

4.1. Limitations of the ADCP variance method

The ADCP measurement of current velocity is based on an assumption of homogeneity, which states that the velocity field must be homogeneous in the horizontal plane over the distances separating the beams (Lu and Lueck, 1999a). To satisfy this requirement, the turbulent eddies must have a length scale larger than the beam separation, or statistically the time mean flow must be horizontally homogeneous over the spatial domain of the beams. The quality of ADCP data, therefore, is often low when the current is weak. In the vertical direction, if the ADCP is used to record velocities with a bin interval of 25 cm, the smallest length scale that can be resolved is 50 cm, and the variances of the measured velocity fluctuations may be reduced if the size of the

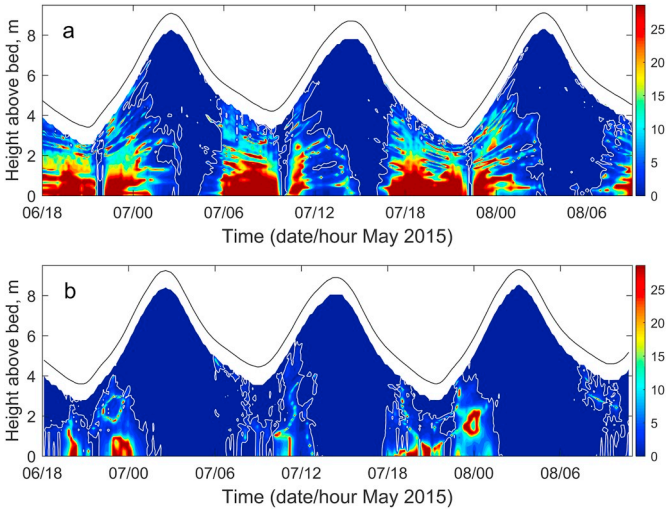

Fig. 8. Temporal variations in profiles of stratification length scale in units of meters defined using shear production and buoyancy frequency ($l_N = \sqrt{P/N^3}$) at stations B (a) and C (b). The white contour lines indicate a value of 1 m.

turbulent eddies is smaller than O(0.5 m) (Stacey et al., 1999b).

The length scale of the largest turbulent eddies in a stably stratified flow is the Ozmidov length scale, which is determined by the magnitude of the stratification and the dissipation rate ε, i.e., $l_O = \sqrt{\varepsilon/N^3}$ (Ozmidov, 1965). Because the dissipation rate was not available in this study, the stratification length scale defined by Stacey et al. (1999b) was used to characterize the theoretical upper bound on the scales of the turbulent motions:

$$l_N = \left(\frac{P}{N^3}\right)^{1/2} \tag{7}$$

This length scale is equivalent to the Ozmidov length scale under the assumption that $P = \varepsilon$. The distribution of the stratification length scale (Fig. 8) showed the influence of stratification on turbulence. During late ebb and early flood, the water column was well mixed and thus $l_N \sim O(10\ \text{m})$. During other phases of the flow, l_N was generally less than 1 m indicating the turbulence is buoyancy limited. At station C, the occurrence of stronger stratification suppressed l_N more than it did at station B.

The smallest possible turbulence length that can be resolved using the ADCP variance method sets a lower bound for the eddy viscosity that can be reliably estimated. At 6 m above the bed (tidal mean water depth), the separation distance between the beams was approximately 4.5 m, indicating that eddies with horizontal scales smaller than 4.5 m cannot be properly resolved. Stacey et al. (1999b) suggested that the horizontal turbulence scale is approximately 5–6 times the vertical scale in an unstratified environment (i.e., the Prandtl mixing length). If we assume that a similar result also holds for the stratified case in the Jiulong River estuary, then the critical vertical eddy length scale is approximately 1.0 m at 6 m above the bed. Fig. 8 shows that l_N mostly satisfies these criteria for the region 0–6 m above the bed during the low-water period at station B, whereas it meets the criteria only for the region 0–4 m above the bed at station C. Therefore, the results during the high-water period presented here, especially those related to the turbulence characteristics at station C, should be interpreted in a more qualitative manner.

4.2. Driving mechanisms of tidal mixing asymmetry

The drivers of tidal mixing asymmetry were examined using the potential energy anomaly (ϕ) method that was developed by Simpson et al. (1990) and further extended to a time-dependent dynamic equation of potential energy anomaly by Burchard and Hofmeister (2008) and de Boer et al. (2008). By diagnosing the terms in this equation, the contributions of various processes to stratification can be identified. The potential energy anomaly equation for the study sites is

$$\frac{\partial \phi}{\partial t} = \frac{g}{D}\int_{-H}^{\eta} \hat{u}\frac{\partial [\rho]}{\partial x} z dz + \frac{g}{D}\int_{-H}^{\eta} [u]\frac{\partial \hat{\rho}}{\partial x} z dz + \frac{g}{D}\int_{-H}^{\eta} K_m \frac{\partial \rho}{\partial z} dz + \frac{g}{D}\int_{-H}^{\eta} \hat{v}\frac{\partial [\rho]}{\partial y} z dz + \frac{g}{D}\int_{-H}^{\eta} [v]\frac{\partial \hat{\rho}}{\partial y} z dz + \cdots, \tag{8}$$

where ϕ is defined as

$$\phi = \frac{1}{D}\int_{-H}^{\eta} gz([\rho] - \rho) dz, \tag{9}$$

and the square brackets indicate the depth average. For example, $[\rho] = \frac{1}{D}\int_{-H}^{\eta} \rho dz$, $\hat{\rho} = \rho - [\rho]$. According to the definition of ϕ, a positive value of ϕ_t indicates increasing stratification. On the right-hand side of Eq. (8), three processes are included and the other terms are omitted due to the lack of data. The first term is the longitudinal straining (also known as tidal straining), the second is the longitudinal advection, the third is the

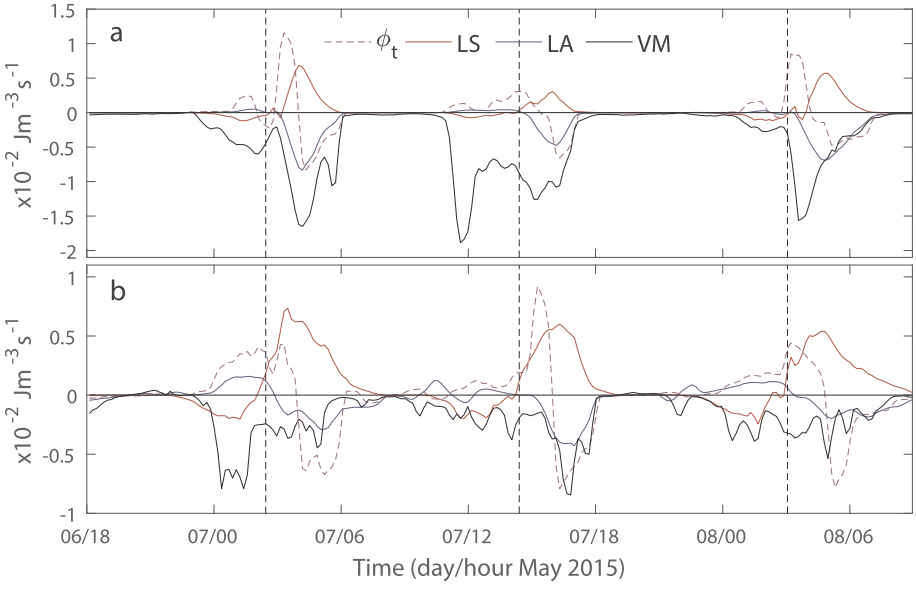

Fig. 9. Major terms in the potential energy anomaly equation at stations B (a) and C (b). LS represents the longitudinal straining, LA represents the longitudinal advection, VM represents the vertical mixing, and ϕ_t indicates the rate of time change in the potential energy anomaly. The vertical dashed lines indicate the times of highest water levels and the vertical dot-dashed lines indicate the times of highest water levels.

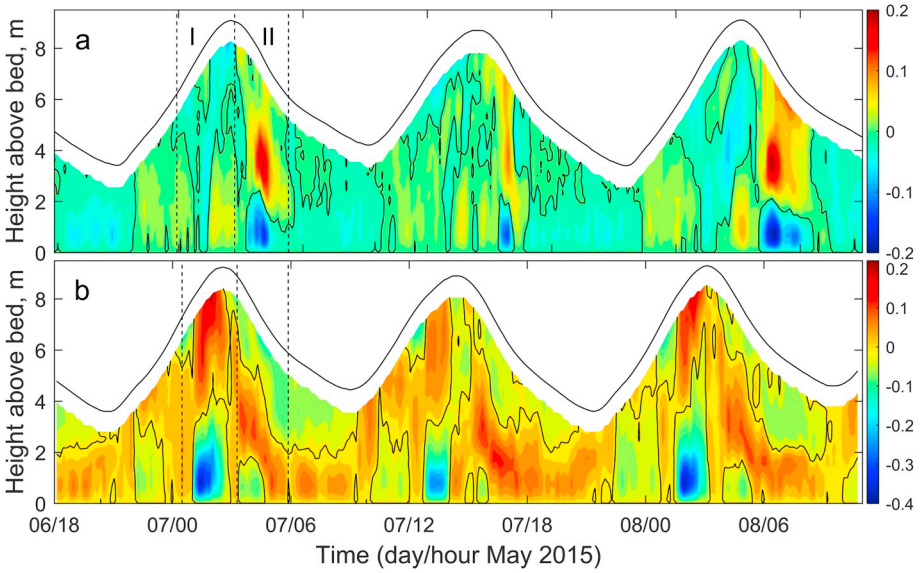

Fig. 10. Temporal variations in profiles of the lateral circulation in units of m/s at stations B (a) and C (b). Positive values indicate rightward (facing upstream) currents. The black contour lines represent a velocity of 0 m/s. The vertical dashed lines illustrate the high-water period of the first tidal cycle; I and II indicate the later flood and early ebb, respectively.

vertical mixing, the fourth term is the lateral straining and the fifth term is the lateral advection. Because the lateral density gradients were not available, we only evaluate the longitudinal processes. The first three terms of Eq. (8) and the left-hand side ϕ_t are plotted in Fig. 9.

The tidal variations of longitudinal straining, longitudinal advection, and vertical mixing showed similar trends at the two stations. Those terms were negligible during the freshwater-dominated low-water period because of the small longitudinal and vertical density gradients, whereas they possessed large values during the saltwater-affected high-water period. The longitudinal straining reduced stratification (negative values) during flood tides and reinforced stratification (positive values) during ebb tides. This result was consistent with the effect of tidal straining on stratification proposed by Simpson et al. (1990) and is similar to that found in the Changjiang River estuary (Pu et al., 2015). The longitudinal advection exerted the opposite effect on stratification compared to the longitudinal straining because it induced the landward advection of stratified water during the flood and the seaward advection of relatively well-mixed water during the ebb. The vertical mixing always destratified the water column. It can be seen that ϕ_t was not equal to the sum of these three terms because of the omission of the other terms in Eq. (8), among which the contribution of lateral circulation in particular may be important. The lateral circulation is addressed in detail in the following section.

4.3. Lateral circulation

The lateral circulation was strong and exhibited relatively clear patterns during the high-water period (Fig. 10). Station B is on the right-hand (north) side of the thalweg. The lateral circulation was generally clockwise (facing upstream) with leftward flow (negative values) near the surface and rightward flow near the bottom during the later flood and generally counterclockwise during the early ebb. This lateral circulation was driven by a lateral baroclinic pressure gradient caused by differential advection when the longitudinal salinity gradient was established upon saltwater intrusion, as also observed by Nunes and Simpson (1985). The strength of the lateral circulation was enhanced during the early ebb resulting from the greater longitudinal salinity gradient (see Fig. 2b).

Station C is on the left-hand (south) side of the thalweg, such that the differential advection induced lateral circulation during the high-water period with the opposite patterns to those at station B. In particular, the lateral circulation was counterclockwise around the maximum flood (i.e., the mean water level, as indicated by the first vertical dashed line in Fig. 10b), which could not be driven by differential advection. As shown in Fig. 1, the part of the estuary channel where station C was located is a concave bend. Therefore, the centrifugal force was responsible for the lateral circulation around maximum flood and also reinforced the lateral circulation during the early ebb tides.

Lateral circulation can make a significant contribution to estuarine dynamics in terms of momentum balance and mixing. Lerczak and Geyer (2004) proposed that when lateral flows are sufficiently strong to advect water parcels a significant distance over a tidal time scale relative to half the channel breadth (i.e., $4|\nu|/\omega W \geq 1$, where ω is the tidal frequency and W is the width of the estuary channel), lateral advection can be expected to play an important role in the longitudinal momentum balance. At station B, the depth-averaged magnitude of lateral circulation ranged from approximately 0.03 to 0.08 m/s during the high-water period, and the resulting $4|\nu|/\omega W$ ranged from 2.8 to 7.6 (here, the M_2 tidal frequency was used, and $W = 300$ m). At station C, the depth-averaged magnitude of lateral circulation ranged from approximately 0.04 to 0.1 m/s during the high-water period, and the resulting $4|\nu|/\omega W$ ranged from 3.8 to 9.5. Therefore, lateral advection had an important influence on the longitudinal dynamics at the two stations.

Lateral circulation modifies stratification in estuaries through straining and advection. To evaluate the importance of lateral straining, the ratio between lateral straining (S_y) and longitudinal straining (S_x) was scaled based on the potential energy anomaly method (referring to Eq. (8))

$$\frac{S_y}{S_x} = \frac{\frac{\partial v}{\partial z}\frac{\partial [\rho]}{\partial y}}{\frac{\partial u}{\partial z}\frac{\partial [\rho]}{\partial x}}. \tag{10}$$

As the cross-channel density was absent in the observation, $\partial[\rho]/\partial y$ was related to the lateral circulation velocity following Lerczak and Geyer (2004), when differential advection dominated the driving forces of lateral circulation

$$v \sim \frac{1}{24}\frac{gH^3}{\rho_0 K_m}\frac{\partial [\rho]}{\partial y}. \tag{11}$$

Combining Eqs. (10) and (11), the ratio becomes

$$\frac{S_y}{S_x} = \frac{24\rho_0 K_m v(\Delta v)}{gH^3 \Delta u \partial[\rho]/\partial x} \quad (12)$$

Here, the vertical velocity difference is scaled as $\Delta u = u_{max} - u_{min}$, and $\Delta v = v_{max} - v_{min}$. For the mean values observed during the high-water period ($H = 7$ m, $\Delta u = 1.0$ m/s, and $\rho_0 = 1.0 \times 10^3$ kg/m^3), this ratio was approximately 1.29 at station B (here, $\partial[\rho]/\partial x = 5.0 \times 10^{-4}$ kg/m^4, $K_m = 3 \times 10^{-3}$ s^{-2}, $v = 0.1$ m/s, and $\Delta v = 0.3$ m/s) and approximately 0.64 at station C (here, $\partial[\rho]/\partial x = 8.0 \times 10^{-4}$ kg/m^4, $K_m = 1.2 \times 10^{-3}$ s^{-2}, $v = 0.15$ m/s, and $\Delta v = 0.4$ m/s), suggesting that lateral advection is important for vertical exchange under stratified conditions. It is noted that the ratio might be slightly overestimated at station C because centrifugal force also contributes to generate lateral circulation such that lateral density gradient might be overestimated using Eq. (11). Lateral advection of potential energy anomaly is related to the vertical density difference. As the CTD measurements were not conducted on shoals, the contribution of lateral advection to the change in the potential energy anomaly was not available. However, shoals in a tidal channel typically have strong vertical mixing, and the lateral gradient of vertical density anomaly is expected to be smaller than its counterpart in the longitudinal direction and therefore less important in determining stratification at the two stations. The analysis indicates that the lateral circulation in the Jiulong River estuary plays an important role in tidal mixing asymmetry and ESCO flow. Consequently, an in-depth examination of lateral circulation is needed and must await future studies.

5. Conclusions

It has been recognized that tidal variation of vertical mixing acts as a driver of estuarine circulation through the eddy viscosity-shear covariance term in the longitudinal momentum equation. To examine the ESCO flow, an observation campaign was carried out at three stations in the inner regime of a tidally energetic estuary. Because of the migration of the saltwater/freshwater interface and the characteristic of standing tidal waves, saltwater was introduced during the high-water period and freshwater dominated the low-water period. The water column was relatively well-mixed during the later flood and was stratified during the early ebb, showing a typical tidal mixing asymmetry. Affected by stratification, the Reynolds stress and vertical eddy viscosity, which were obtained using the ADCP variance method, exhibited distinct differences in magnitude and vertical structure between flood and ebb tides. Using the decomposition method for estuarine circulation, two components of residual flow were obtained at two of the observation stations. The ESCO flow possessed a two-layer vertical structure and a considerably greater strength than the density-driven flow, supporting the findings of generic model studies that the ESCO flow dominates the density-driven flow in periodically stratified estuaries.

The drivers of tidal mixing asymmetry were examined using the potential energy anomaly method. The results showed that longitudinal straining reduced stratification during the flood tides and reinforced stratification during the ebb tides, which is consistent with the effects of tidal straining on stratification. Longitudinal advection exerted the opposite effect on stratification and vertical mixing always destratified the water column. The contribution of lateral circulation to stratification was neglected due to the lack of lateral observation data. However, a scaling analysis of the lateral circulation revealed that lateral advection was crucial for the longitudinal dynamics and the influence of lateral straining on stratification was as important as that of longitudinal straining. Further study of the lateral circulation is required to examine its role in generating ESCO flow. The ADCP variance method is based on an assumption of homogeneity, which requires that the turbulent eddies possess a length scale larger than the beam separation and bin size. Examination of the stratification length scale, which represents the largest scale of turbulent eddies, revealed that the turbulent eddies were not sufficiently large during slack water and the stratified early ebb tides, particularly at station C, and the interpretation of the data for these periods was therefore limited to a qualitative analysis.

Declaration of competing interest

All authors declare that we have no financial and personal relationships with other people or organizations that can inappropriately influence our work, there is no professional or other personal interest of any nature or kind in any product, service and/or company that could be construed as influencing the position presented in, or the review of, the manuscript entitled.

Acknowledgements

P. Cheng thanks the financial support from the National Natural Science Foundation of China (grant no. 41476004), and the National Basic Research Program of China (grant no. 2015CB954000). F. Yu thanks the financial support from the Youth Program of National Natural Science Foundation of China (grant no. 41706039). N. Chen thanks the financial support from the National Natural Science Foundation of China (grant no. 41676098) and Fundamental Research Funds for the Central Universities (20720160120, 20720180119). A. Wang thanks the financial support from the National Natural Science Foundation of China (grant no. 41376070). We thank Gaoyang Li, Fangtao Zhang and the crew of the R/V Ocean II for their assistance on the cruises. The in situ data used in this study are available upon request from P. Cheng (pcheng@xmu.edu.cn). We thank three anonymous reviewers for their insightful comments that helped improve this work.

References

Becherer, J., Burchard, H., Flöser, G., Mohrholz, V., Umlauf, L., 2011. Evidence of tidal straining in well-mixed channel flow from micro-structure observations. Geophys. Res. Lett. 38, 2–6. https://doi.org/10.1029/2011GL049005.

Burchard, H., Hofmeister, R., 2008. A dynamics equation for the potential energy anomaly for analyzing mixing and stratification in estuaries and coastal seas. Estuar. Coast Shelf Sci. 77, 679–687. https://doi.org/10.1016/j.ecss.2007.10.025.

Burchard, H., Schuttelaars, H.M., 2012. Analysis of tidal straining as driver for estuarine circulation in well-mixed estuaries. J. Phys. Oceanogr. 42, 261–271. https://doi.org/10.1175/JPO-D-11-0110.1.

Burchard, H., Hetland, R.D., 2010. Quantifying the contributions of tidal straining and gravitational circulation to residual circulation in periodically stratified tidal estuaries. J. Phys. Oceanogr. 40, 1243–1262. https://doi.org/10.1175/2010JPO4270.1.

Chen, W., de Swart, H.E., 2018. Estuarine residual flow induced by eddy viscosity-shear covariance: dependence on axial bottom slope, tidal intensity and constituents. Cont. Shelf Res. 167, 1–13. https://doi.org/10.1016/j.csr.2018.07.011.

Cheng, P., Valle-Levinson, A., de Swart, H.E., 2010. Residual currents induced by asymmetric tidal mixing in weakly stratified narrow estuaries. J. Phys. Oceanogr. 40, 2135–2147. https://doi.org/10.1175/2010JPO4314.1.

Cheng, P., De Swart, H.E., Valle-Levinson, A., 2013. Role of asymmetric tidal mixing in the subtidal dynamics of narrow estuaries. J. Geophys. Res. Oceans 118, 2623–2639. https://doi.org/10.1002/jgrc.20189.

de Boer, G.J., Pietrzak, J.D., Winterwerp, J.C., 2008. Using the potential energy anomaly equation to investigate tidal straining and advection of stratification in a region of freshwater influence. Ocean Model. 22, 1–11. https://doi.org/10.1016/j.ocemod.2007.12.003.

Dijkstra, Y.M., Schuttelaars, H.M., Burchard, H., 2017. Generation of exchange flows in estuaries by tidal and gravitational eddy viscosity-shear covariance (ESCO). J. Geophys. Res. Oceans 122, 4217–4237. https://doi:10.1002/2016JC012379.

Friedrichs, C.T., Aubrey, D.G., 1988. Non-linear tidal distortion in shallow well-mixed estuaries: a synthesis. Estuar. Coast Shelf Sci. 38, 157–172. https://doi.org/10.1016/0272-7714(88)90082-0.

Geyer, W.R., Trowbridge, J.H., Bowen, M.M., 2000. The dynamics of a partially mixed estuary. J. Phys. Oceanogr. 30, 2035–2048.

Hansen, D.V., Rattray, M., 1965. Gravitational circulation in straits and estuaries. J. Mar. Res. 23, 104–122.

Jay, D.A., 1991. Internal asymmetry and an harmonicity in estuarine flows. In: Parker, B. B. (Ed.), Process in Tidal Hydrodynamics. John Wiley & Sons Inc., New Jersey, pp. 521–546.

Jay, D.A., Musiak, J.D., 1994. Particle trapping in estuarine tidal flows. J. Geophys. Res. 99, 445–461. https://doi.org/10.1029/94JC00971.

Jiang, Y.W., Wai, O.W.H., 2005. Drying–wetting approach for 3D finite element sigma coordinate model for estuaries with large tidal flats. Adv. Water Resour. 28, 779–792. https://doi:10.1016/j.advwatres.2005.02.004.

Lerczak, J.A., Rockwell Geyer, W., 2004. Modeling the lateral circulation in straight, stratified estuaries. J. Phys. Oceanogr. 34, 1410–1428. https://doi.org/10.1109/RAST.2003.1303919.

Liu, W., Chen, F., Zhou, D., 1994. Formation and evolution of the shoal estuarine channel to Haichang Harbour, Xiamen. J. Oceanogr. Taiwan Strait 13, 317–322 (in Chinese with an English abstract).

Lu, Y., Lueck, R.G., 1999a. Using a broadband ADCP in a Tidal Channel. Part I: mean flow and shear. J. Atmos. Ocean. Technol. 16, 1556–1567. https://doi.org/10.1175/1520-0426(1999)016<1556:UABAIA>2.0.CO;2.

Lu, Y., Lueck, R.G., 1999b. Using a broadband ADCP in a Tidal Channel. Part II: turbulence. J. Atmos. Ocean. Technol. 16, 1568–1579. https://doi.org/10.1175/1520-0426(1999)016<1568:UABAIA>2.0.CO;2.

Nunes, R.A., Simpson, J.H., 1985. Axial convergence in a well-mixed estuary. Estuar. Coast Shelf Sci. 20, 637–646. https://doi.org/10.1016/0272-7714(85)90112-X.

Ozmidov, R.V., 1965. On the turbulence exchange in a stably stratified ocean. Atmos. Oceanic Phys. Ser. 1, 493–497.

Pritchard, D.W., 1956. The dynamic structure of a coastal plain estuary. J. Mar. Res. 15, 33–42.

Pu, X., Shi, J.Z., Hu, G.-D., Xiong, L.-B., 2015. Circulation and mixing along the North passage in the Changjiang River estuary, China. J. Mar. Syst. 148, 213–235.

Simpson, J.H., Brown, J., Matthews, J., Allen, G., 1990. Stirring in the control of estuarine stratification. Estuaries 13, 125–132. https://doi.org/10.2307/1351581.

Simpson, J.H., Williams, E., Brasseur, L.H., Brubaker, J.M., 2005. The impact of tidal straining on the cycle of turbulence in a partially stratified estuary. Cont. Shelf Res. 25, 51–64. https://doi.org/10.1016/j.csr.2004.08.003.

Stacey, M.T., Monismith, S.G., Burau, J.R., 1999a. Measurements of Reynolds stress profiles in unstratified tidal flow. J. Geophys. Res. Oceans 104, 10933–10949. https://doi.org/10.1029/1998JC900095.

Stacey, M.T., Monismith, S.G., Burau, J.R., 1999b. Observation of turbulence in a partially stratified estuary. J. Phys. Oceanogr. 29, 1950–1970. https://doi.org/10.1175/1520-0485(1999)029<1950:OOTIAP>2.0.CO;2.

Stacey, M.T., Ralston, D.K., 2005. The scaling and structure of the estuarine bottom boundary layer. J. Phys. Oceanogr. 35, 55–71. https://doi.org/10.1175/JPO-2672.1.

Wang, Y.P., Voulgaris, G., Li, Y., Yang, Y., Gao, J., Chen, J., Gao, S., 2013. Sediment resuspension, flocculation, and settling in a macrotidal estuary. J. Geophys. Res. Oceans 118. https://doi:10.1002/jgrc.20340.